STRUCTURAL SCIENCE
CRYSTAL ENGINEERING
MATERIALS

ISSN: 2052-5206
journals.iucr.org/b

Compressibility of structural modulation waves in the chain compounds BaCoX_2O$_7$ (X = As, P): a powder study

Ranjana R. Das, Bastien Leclercq, Pierre Bouvier, Angel M. Arévalo-López, Céline Goujon, Jean-Paul Itié, Alain Polian, Olivier Mentré and Claire V. Colin

Acta Cryst. (2022). B**78**, 162–171

STRUCTURAL SCIENCE
CRYSTAL ENGINEERING
MATERIALS

ISSN 2052-5206

Compressibility of structural modulation waves in the chain compounds $BaCoX_2O_7$ (X = As, P): a powder study

Ranjana R. Das,[a] Bastien Leclercq,[b] Pierre Bouvier,[a] Angel M. Arévalo-López,[b] Céline Goujon,[a] Jean-Paul Itié,[c] Alain Polian,[d,c] Olivier Mentré[b] and Claire V. Colin[a]*

[a]Institut Néel, Université Grenoble Alpes, CNRS, Grenoble, 38042, France, [b]UCCS (Unité de Catalyse et Chimie du Solide), CNRS UMR 8181, Bâtiment C7, Univ. Lille - Centrale Lille/ENSCL, Avenue Mendeleiev, 59655 - Villeneuve d'Ascq, France, [c]Synchrotron SOLEIL, L'Orme des Merisiers, St Aubin BP48, Gif sur Yvette Cedex, 91192, France, and [d]Institut de Minéralogie, de Physique des Matériaux et de Cosmochimie, CNRS UMR 7590, Sorbonne Université, 4 Place Jussieu, Paris, 75005, France. *Correspondence e-mail: claire.colin@neel.cnrs.fr

Received 8 September 2021
Accepted 1 February 2022

Edited by P. Bordet, Institut Néel, France

Keywords: incommensurate structural modulation; first-order structural phase transition; high-pressure Raman spectroscopy; high-pressure X-ray diffraction; DFT-relaxed structural models.

Supporting information: this article has supporting information at journals.iucr.org/b

$BaCoX_2O_7$ (X = As, P) are built on magnetic 1D units in which strong aperiodic undulations originate from incommensurate structural modulations with large atomic displacive amplitudes perpendicular to the chain directions, resulting in very unique multiferroic properties. High-pressure structural and vibrational properties of both compounds have been investigated by synchrotron X-ray powder diffraction and Raman spectroscopy at room temperature and combined with density functional calculations. A structural phase transition is observed at 1.8 GPa and 6.8 GPa in $BaCoAs_2O_7$ and $BaCoP_2O_7$, respectively. Sharp jumps are observed in their unit-cell volumes and in Raman mode frequencies, thus confirming the first-order nature of their phase transition. These transitions involve the disappearance of the modulation from the ambient-pressure polymorph with clear spectroscopic fingerprints, such as reduction of the number of Raman modes and change of shape on some peaks. The relation between the evolution of the Raman modes along with the structure are presented and supported by density functional theory structural relaxations.

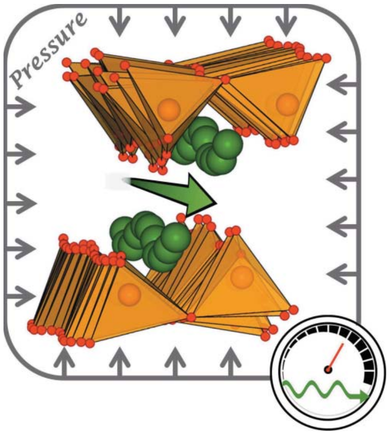

1. Introduction

The physics of $BaCo(X_2O_7)$ (X = P, As) quasi one-dimensional (1D) magnetic materials is governed by a strong spin–spin coupling along the 1D-direction, together with much weaker exchange along the other directions (David *et al.*, 2013). In the case of highly anisotropic spins such as Co^{2+} in the chain-like units, field-induced phenomena such as metamagnetic transitions aligning isolated magnetic units (Lenertz *et al.*, 2014; Singh *et al.*, 2012) or incommensurate spin density waves may occur (Canévet *et al.*, 2013) with interesting theoretical insights. The possibility of enhanced magnetoelectric exchanges along magnetization steps have attracted considerable attention. In that context, the low-dimensional compounds α-$BaMX_2O_7$ (M = Co, Ni, Fe; X = P, As) are relevant cases due to their incommensurately modulated structures with large atomic displacive waves (Riou *et al.*, 1988). They consist of one-dimensional (1D) antiferromagnetic (AFM) chains undulated by the incommensurate modulation, giving a mixed 1D/2D 'real' magnetic topology with a metamagnetic scenario. In $BaCoX_2O_7$, the modulated distribution of Ising-spin exchanges induces a magnetic complex phase diagram with competition between collinear AFM, charge density wave (CDW) and ferromagnetic (FM) structures increasing the applied field. An original mechanism at the origin of the multiferroicity in these compounds was proposed recently (Leclercq *et al.*, 2021). The spin-induced ferroelectric phase results from a unique combination of the atomic waves, the collinear magnetic structure and magnetic dipole–dipole interactions. As the magnetic and multiferroic properties of these series are strongly correlated with their incommensurately undulated structures, a deeper understanding of the pressure effect was investigated. Indeed, the investigation of the compressibility of the atomic displacive waves propagated along the 1D chains associated with large atomic displacement appear as a relevant structural research area. One attractive property of high pressure is its character as a 'cleaner' variable compared to other parameters such as temperature since it acts only on interatomic distances, and not on either chemical or entropic changes. Here we established the relationship between pressure-induced phase changes and the vibrational properties by a systematic study of the pressure dependence of X-ray diffraction (XRD) synchrotron data and Raman spectra in α-$BaCoAs_2O_7$ (BCAO) and α-$BaCoP_2O_7$ (BCPO). It has been analysed using complementary relaxed structural models obtained by density functional theory (DFT), giving serious arguments for the disappearance of incommensurate structural modes at the transition.

2. Experimental and calculation methods

The details of polycrystalline sample synthesis procedures by solid-state reaction at high temperature were reported elsewhere (David *et al.*, 2013; Leclercq *et al.*, 2021).

Preliminary laboratory X-ray measurements under pressure were carried out in transmission geometry at the Institut Néel (Grenoble). The set-up consists of a micro-focused Ag X-ray source ($\sim$0.56 Å) and a 2D Mar 345 detector. The powder samples were loaded in a membrane diamond anvil cell (DAC) using a 60 µm-thick rhenium gasket with a 250 µm pressure chamber and a 500 µm bevelled diamond culet. A methanol–ethanol (4:1) mixture was used as the pressure-transmitting medium (PTM). A ruby ball, loaded near the sample, was used for pressure calibration. We note that complementary measurements on single crystals are out of the scope of this work, dedicated to preliminary powder study.

The synchrotron diffraction study was carried out at PSICHÉ beamline at Synchrotron SOLEIL, Paris, using monochromatic radiation of $\lambda = 0.3738$ Å. The beam size was 20 µm. Diffraction patterns were collected using a PILATUS3 X 2M CdTe detector. Precise calibration of the detector parameters was extracted with a reference sample of CeO_2 powder, and retrieval of conventional 2θ-intensity data was carried out with the *DIOPTAS* software (Prescher & Prakapenka, 2015). The powder samples were loaded in a DAC with diamond tips of diameters 300 µm and 400 µm with a stainless steel gasket (thickness: 30 µm, hole diameter: 150 µm) along with Daphne oil and neon as a PTM for BCAO and BCPO, respectively. The choice of PTM was made based on their hydrostatic properties in the measured pressure range. Daphne oil is a well adapted PTM with a good hydrostaticity in the low-pressure regime (up to 5 GPa). Neon gas has a low-pressure gradient up to much higher pressure and was better suited for the exploration of BCPO up to 18 GPa (Klotz *et al.*, 2009). Calibration of pressure was carried out *in situ* by measuring the diffraction lines of gold powder. The powder diffraction data were analyzed by Lebail fitting using the *FullProf* software (Rodríguez-Carvajal, 2001). The unit-cell parameter refinement from *HKL*s were performed using the *CELREF* software (Laugier & Bochu, 2002). In all Le Bail refinements, the background was specified by linear interpolation of selected points in the pattern, and the Thomson–Cox–Hastings model function was used for the profile function (Finger *et al.*, 1994). *Vesta* software (Momma & Izumi, 2008) was used for structural visualization and crystallographic analysis.

High-pressure Raman spectroscopy measurements were done on freshly ground powder loaded into a membrane DAC equipped with bevelled anvils having 350/400 µm culet tips. A 50 µm-thick stainless-steel gasket was drilled to obtain a 150 µm pressure chamber. A methanol–ethanol (4:1) mixture was used as the PTM because this mixture retains weak Raman activity and ensures quasi-hydrostatic conditions up to 10 GPa in the pressure cell. A ruby ball loaded close to the sample was used for pressure calibration at room temperature using the R1-line emission (Holzapfel, 2003). The degradation of the homogeneity of the DAC pressure was followed from the half-width at half maximum of one R1 ruby line. The ruby and Raman measurements were carried out at room temperature with a 514.4 nm (Cobolt Fandango) laser and a spectrometer made of an ACTON Spectra Pro 2750 monochromator with an 1800 mm^{-1} grating (blazed at 500 nm), equipped with a Pylon eXcelon CCD camera, and a 50 µm entrance slit size that provides a resolution of 1.09 cm^{-1} (0.03 nm). A set of three Bragg filters (BNF Optigrate) were used in order to reject the excitation line to a 25 cm^{-1} relative wavenumber cutoff. The spectra were recorded in back-scattering geometry with a 40× objective (Nikon) to focus the incident laser beam and to collect the scattered light inside the DAC through the diamond anvil. The spectrometer was calibrated in wavenumber by using the lines of the Princeton Instrument Ne-Ar lamp. The measurements were carried out with an incident laser power of 10 mW on the DAC. The laser power was fixed in order to avoid any influence of laser heating on the Raman spectra. The Raman spectra covering a 25–1250 cm^{-1} spectral range are recorded in two monochromator positions with 60 s acquired time-averaged over five acquisitions. Spectral parameters (position and half-width at half maximum) were obtained from the decomposition of each spectrum with several Lorentzian peaks using *Fityk* software (version 1.3.1; Wojdyr, 2010).

Density functional theory (DFT) calculations were performed using the projector augmented-wave method (Blöchl, 1994) implemented in the Vienna *ab initio* Simulation Package (*VASP*) (Kresse *et al.*, 2012), with the full-potential local-orbital scheme (FPLO9.00-33; Koepernik & Eschrig, 1999). We used the generalized gradient approximation for electron exchange and correlation corrections (Perdew *et al.*, 1996). The cutoff energy for the planewave expansion was 550 eV, and reciprocal-space integration was performed on $6 \times 4 \times 4$ for the a, b, c subcell ($2 \times 4 \times 2$ for the $7a$, b, $2c$ supercell) Monkhorst-pack meshes. It included 52 and 12 k-points in the symmetry-irreducible part of the first Brillouin zone, respectively. Convergence criteria of 10^{-7} eV, 3×10^{-4} eV Å^{-1} and 10^{-5} eV, 3×10^{-2} eV Å^{-1} were set for convergence of the electronic cycles and ionic relaxation, respectively.

3. Results and discussions

3.1. Crystal structure

The average crystal structures of $BaCoX_2O_7$ (X = As, P, hereafter BCAO and BCPO) and also $BaFeP_2O_7$ were determined previously from single-crystal diffraction by Riou *et al.* (1988), David *et al.* (2013) and Leclercq *et al.* (2021). All compounds crystallize in the triclinic symmetry (space group $P\bar{1}$, $Z = 2$) as shown in Fig. 1(*a*). The average structure consists of infinite chains of edge-sharing Co_2O_8 square pyramid dimers running along the a axis, connected by pyro-arsenates As_2O_7 or pyro-phosphates P_2O_7 bridges. They form planes of parallel chains in the (a,c) plane, stacked along the b axis and separated by Ba^{2+} cations. The incommensurate modulations with $P\bar{1}(\alpha, \beta, \gamma)0$ superspace groups, given the modulation propagation vectors $\mathbf{q}$ $[0.13571\ (4), 0.0781\ (1), 0.4768\ (1)]_{\rm BCAO}$ and $[0.146\ (4),\ 0.075\ (2),\ 0.470\ (2)]_{\rm BCPO}$, were refined from single crystal XRD at room temperature (David *et al.*, 2013). Thus, the modulated structure may be assimilated to a rational $7a \times b \times 2c$ supercell approximant for further DFT calculations experiments. The main atomic displacement occurs along the $\mathbf{c}$, *i.e.* between individual chains in the ac plane, such that strongly undulated chains are connected or not into pseudo-2D lattices. The Co—O7 bond distance is one of the most modulated and varies between $\simeq 2.2$ and $\simeq 3.7$ Å. It returns locally with CoO_5 or CoO_6 polyhedra, as shown in Fig. 1(*c*). The undulation is also mediated by the modulated bending of the X_2O_7 groups [see Fig. 1(*b*)]. Figs. 1(*d*) and 1(*e*), discussed below, correspond to DFT-relaxed structures starting from our synchrotron refined structures at 0.55 GPa and 3.6 GPa, respectively. Once again, the compressibility of such undulated chains deserves particular attention, also at the origin of this study.

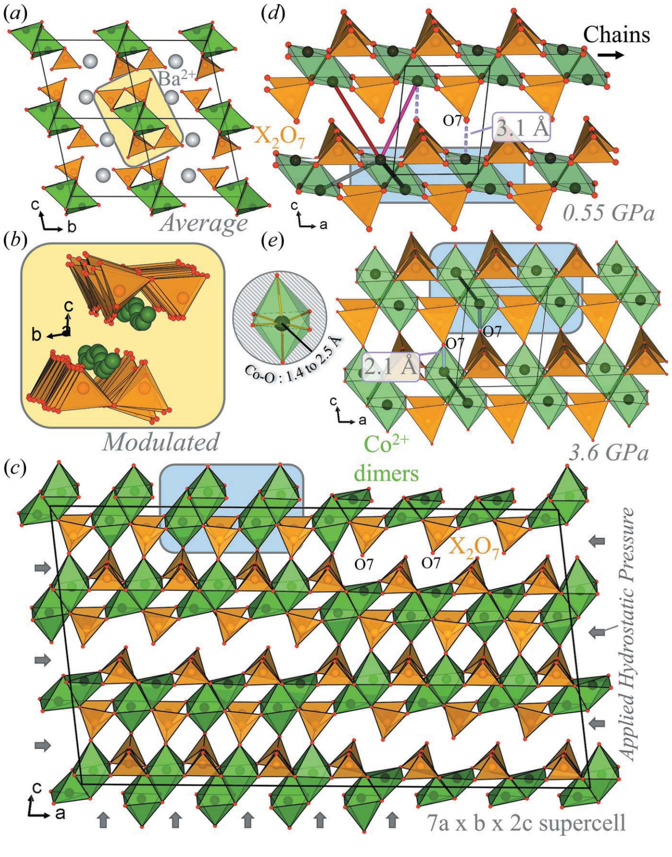

Figure 1
(*a*) Representation of the average structure of $BaCoX_2O_7$ (X = P, As) structure ($P\bar{1}$) and (*b*), (*c*) overviews of the related modulated structure [$P\bar{1}(\alpha, \beta, \gamma)0$], assimilated to a $7a \times b \times 2c$ supercell. (*d*), (*e*) Projections of structures obtained from DFT relaxation calculations at an applied pressure of 0.55 and 3.6 GPa, respectively. Co—O bond lengths were considered up to 2.5 Å. Co^{2+} atoms and polyhedra are represented in green colour while pyro-arsenate and phosphate X_2O_7 are in orange. Ba^{2+} atoms are light grey.

3.1.1. Synchrotron diffraction. Preliminary laboratory X-ray diffraction experiments up to 16 GPa were carried out at Institut Néel. See Figs. S1 and S2 in supporting information for plots of the evolution of unit-cell parameters versus applied pressure, according to refined values reported in Tables S1 and S2. Despite the lower resolution of the diffraction pattern in the laboratory set-up, the average pressures of structural transitions were identified by the evolution of the unit-cell parameters and the pressure range was adapted for synchrotron measurements.

Figs. 2(*a*) and 2(*b*) (for BCAO and BCPO, respectively) show selected synchrotron X-ray diffraction patterns measured on BCAO and BCPO up to 5.1 GPa and up to 18.65 GPa, respectively. We found that all patterns collected from ambient pressure with laboratory X-ray set-up to the highest pressure measured in synchrotron X-ray diffraction can be indexed in the parent triclinic symmetry with important parameters shifting from their original values. The quality of

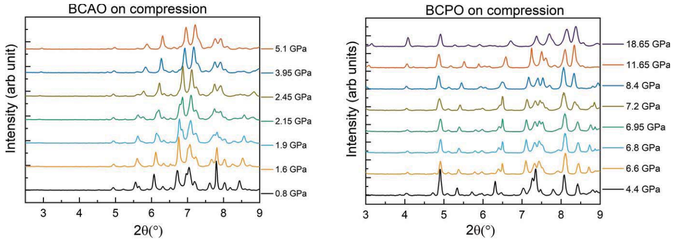

(*a*) (*b*)

Figure 2
(*a*) Synchrotron X-ray diffraction patterns of BCAO from 0.8 GPa up to 5.1 GPa at room temperature on compression. (*b*) Synchrotron X-ray diffraction patterns of BCPO from 4.4 GPa up to 18.65 GPa at room temperature on compression.

the synchrotron X-ray diffraction (SXRD) patterns allows for the Le Bail structural refinements from 0.55 to 5.2 GPa in BCAO and from 4.4 to 18.65 GPa in BCPO. However, the data quality was not sufficient to perform a full structural Rietveld refinement because the 2D detector images show very spotty rings and the extracted peak intensity were not reliable due to poor powder averaging. Furthermore, the very low intensity satellites from modulation were not observable on either laboratory or synchrotron powder XRD and the Le Bail fits were done considering the average structure model only.

We refined the synchrotron XRD patterns in the triclinic average cell with $P\bar{1}$ space group using the Le Bail method, which allows us to extract the evolution of the unit-cell parameters under compression and decompression. We used the refined unit-cell parameters obtained from the ambient pressure data recorded outside the DAC at the laboratory source. While performing systematic and iterative refinement, we find it exceedingly difficult to refine the high-pressure synchrotron X-ray diffraction pattern by considering the previous pressure refined parameters around the phase transition, where many peak positions were not accounted for the structure. To solve this problem, we indexed the pattern manually, considering the trend of specific reflections with pressure. It can be more easily visualized through a 2D colour map of the pressure dependence synchrotron data of BCAO and BCPO as shown in Figs. 3(*a*) and 3(*b*), respectively (*xy* plots stacked with an offset are also available in Fig. S5 in supporting information).

3.1.2. Evidence of a high-pressure-induced first-order transition. The indexing of the SXRD pattern *versus* pressure is plotted in Fig. 3(*a*) BCAO and Fig. 3(*b*) BCPO. We observed abrupt peak shifts around ~2 GPa in BCAO and ~7 GPa in BCPO, exaggerated at (002) and (120) diffraction positions. It suggests a first-order phase transition together with non-linear lattice compression at these critical pressures (Fig. 4). The first-order nature of this transition is further supported by the co-presence of the two phases in competition in a range, ΔP ~0.7 GPa, around the transition: 1.8–2.55 GPa in BCAO and 6.8–7.45 GPa in BCPO on compression, see Fig. S4 in supporting information. The peaks shift to the higher angle with increasing pressure except for the (200) peak that evolves oppositely, denoting a strong anisotropic pressure effect at the transition. Experimentally, to account for all the peak positions of $P\bar{1}$ in the refinement, we first refined the unit-cell parameters using *CELREF* software (Laugier & Bochu, 2002) at each pressure point. Then these parameters were used in LeBail refinement using *FullProf* software. It is worth noting that we have checked unsuccessfully for any higher symmetry above the transition.

The evolution of the unit-cell parameters and unit-cell volumes on compression of BCAO and BCPO are presented in Figs. 4(*a*) and 4(*b*), respectively. These values obtained from synchrotron experiments present an excellent overall agreement with the parameters obtained from laboratory-based X-ray diffraction (see Figs. S1 and S2).

The unit-cell parameters and unit-cell volumes decrease continuously with pressure up to 1.8 GPa for BCAO and up to 6.8 GPa for BCPO. Then an abrupt change in parameters and a volume collapse is observed, indicating the onset of a first-order phase transition. Although the difference in critical pressure between the pyro-phosphates and the pyro-arsenates compounds is significant, their signatures are quite similar in terms of anisotropy, as detailed below. We could suggest that inorganic arsenates are less compressible before critical phase transition than phosphates for steric reasons [rP^{5+}(IV) = 0.17 Å versus rAs^{5+}(IV) = 0.34 Å]. For instance, it was shown recently that 'ambient pressure' $BiCu_2O_2(PO_4)$ (Colmont *et al.*, 2018) and $BiNiO(PO_4)$ (Colmont *et al.*, 2021) can be

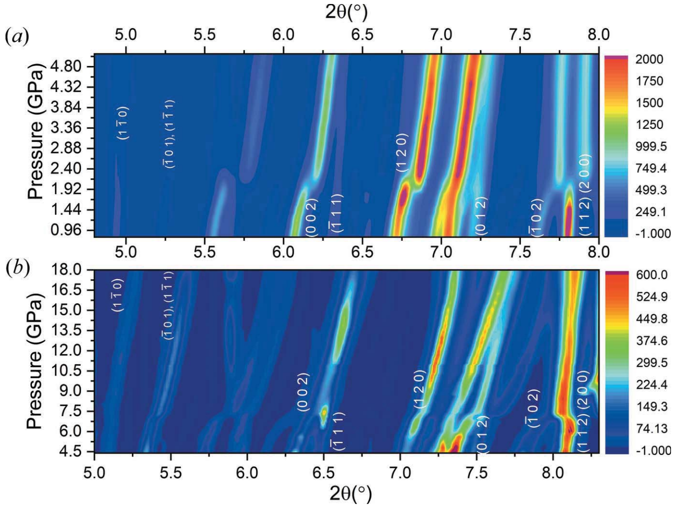

Figure 3

Two-dimensional map of pressure evolution of synchrotron diffraction pattern for (*a*) BCAO and (*b*) BCPO with their most substantial Bragg peaks indexed. The colour scale represents the X-ray diffracted intensity. It clearly shows the existence of first-order phase transition around 1.88 GPa for BCAO and 6.8 GPa for BCPO.

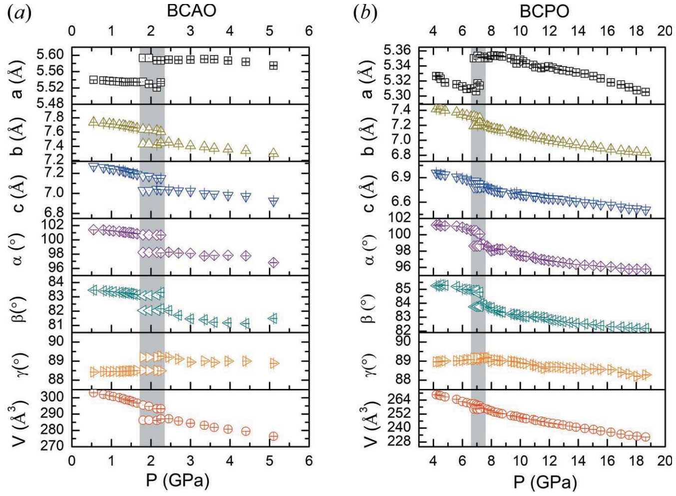

Figure 4

Pressure evolution for unit-cell parameters of triclinic space group $P\bar{1}$ with *a*, *b*, *c*, angles *α*, *β*, *γ* and volume *V* of the unit cell represented from top to bottom for (*a*) BCAO and (*b*) BCPO on compression. The grey shaded region indicates the coexistence of low-pressure and high-pressure phases. Errors along *y* axes are smaller than the symbols.

transformed into 'high-pressure' polymorphs at high pressure, these latter being both isomorphs of the 'ambient pressure' arsenates analogs, $BiCu_2O_2(AsO_4)$ and $BiNiO(AsO_4)$. These two cases show the greater compactness of inorganic arsenates in comparison with phosphate equivalent materials, which are more prone to structural transition under pressure. The two-phases areas are highlighted in the grey shaded regions for BCAO and BCPO in Figs. 4(*a*) and 4(*b*), respectively. Some points in these regions of coexisting phases were kept constant to avoid divergence issues during the refinement. The diffraction patterns collected on decompression for BCAO and BCPO samples indicate complete reversibility of the phase transition. The extracted unit-cell parameters for the resulting refinements on decompression (displayed Fig. S3) corroborated well with the compressibility data. The extracted unit-cell parameters information of the low pressure (LP) and high pressure (HP) phases of BCAO and BCPO are given in Tables S3 and S4, and plotted in Fig. S3. There are two significant points to notice. (*a*) In compression, the unit-cell parameters continuously decrease up to the critical pressure P_c. (*b*) At the phase transition from LP to HP, we see a positive jump of a and γ, with +1.05%; +0.78% in BCAO at P_c = 1.8 GPa, and with +0.75%; +0.1% in BCPO at P_c = 6.8 GPa, respectively, whereas at the same pressure the other unit-cell parameters (*i.e.* b, c, α and β) show a decreasing jump with 2.7%, 2.02%, 2.4% and 1.25% for BCAO, and 1.7%, 1.1%, 1.9%, 1.4% for BCPO, respectively. Moreover, the unit-cell volume of BCAO and BCPO keeps decreasing continuously up to P_c where an abrupt drop of 3.14% and 1.76%, respectively, occurs as shown previously in the grey region in Fig. 4.

Hence this implies that the compressibility of BCAO and BCPO is strongly anisotropic; the lattice is more compressible along the b and c axis, but less along the a direction.

3.1.3. Determination of the equation of state. We have analyzed the pressure–volume (P–V) data obtained from the experiments using a second-order Birch—Murnaghan equation of state (EOS) to calculate the bulk modulus. The fit was performed using the *EosFit7* software by fixing the derivative of the bulk modulus K_p = 4 (Gonzalez-Platas *et al.*, 2016). From the fit, we find the bulk modulus at zero pressure K_0 and zero pressure volume V_0. In Fig. 5, the solid line shows the fit to the data for the LP phase, and the dashed line shows the fit to the volume data for the HP phase from the experiment: (*a*) BCAO K_0 = 44 (4) GPa, V_0 = 307.6 (8) Å^3 (LP phase), K_0 = 57 (3) GPa, V_0 = 298.5 (8) Å^3 (HP phase) and (*b*) BCPO K_0 = 62 (3) GPa, V_0 = 285.5 (9) Å^3 (LP phase) and K_0 = 67.7 (7) GPa, V_0 = 280.2 (2) Å^3 (HP phase). The deduced bulk moduli values are similar to those obtained for some other oxide materials such as cubic ZrP_2O_7 (39 GPa), (Carlson & Krogh Andersen, 2001) cubic TiP_2O_7 (42 GPa) (Carlson & Krogh Andersen, 2001), quasi one-dimensional cuprate Sr_2CuO_3 (92 GPa) (Hyatt *et al.*, 2004), or also $SrCuO_2$ (88 GPa) (Hyatt *et al.*, 2004), respectively.

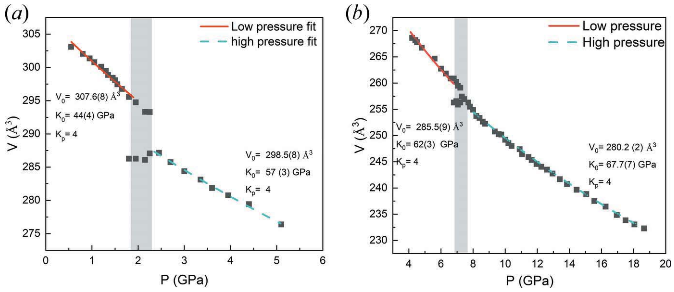

Figure 5

The unit-cell volume as a function of pressure is shown. The red solid line shows a fit to the data for the low-pressure phase and the blue dashed line shows a fit to the data for the high-pressure phase from the experiment using a second-order Birch–Murnaghan equation of state: (*a*) BCAO K_0 = 44 (4) GPa, V_0 = 307.6 (8) Å^3 (low-pressure phase), BCAO K_0 = 57 (3) GPa, V_0 = 298.5 (8) Å^3 (high-pressure phase) and (*b*) BCPO K_0 = 62 (3) GPa, V_0 = 285.5 (9) Å^3 (low-pressure phase) and BCPO K_0 = 67.7 (7) GPa, V_0 = 280.2 (2) Å^3 (high-pressure phase). The grey shaded region is the coexistence of low- and high-pressure phase regions.

From the analysis of the synchrotron diffraction data we can conclude:

(*a*) The onset of the phase transition occurs at P_c = 1.8 GPa for BCAO and 6.8 GPa for BCPO.

(*b*) The phase transitions are first order in $BaCoX_2O_7$ (X = As, P) compounds.

(*c*) Phase transitions are reversible for both compounds.

(*d*) At the transition, the compression is strongly anisotropic with an unusual cell-expansion along a.

We have performed DFT calculations and Raman spectroscopy studies to understand the vibrational properties of these compounds under hydrostatic pressure.

3.1.4. Structural features versus the pressure. In the absence of reliable refined *in situ* structural models during the experiment under pressure, we used DFT-relaxed structural models constraining the accurate refined lattice parameters from our synchrotron XRD experiments.

In a first set of calculations, we used the average primitive cell of BCAO (1 × a, 1 × b, 1 × c) as reported from single-crystal data, assuming that the average cell corresponds to an energy minimum. Seven models have been selected including the LP and HP polymorphs as follows: $[1.10^{-3}$ GPa, 0.55 GPa, 1.35 GPa, 2.25 GPa$]_{LP}$ and [2.25 GPa, 3.6 GPa, 5.1 GPa$]_{HP.}$ All models converged promptly which validates their significance at the average primitive cell level. Although the relaxation is performed in the $P1$ space group, no significant deviation from the centrosymmetric $P\overline{1}$ symmetry occurred during the ionic relaxation steps. Figs. 1(*d*) and 1(*e*) show two projections of the relaxed structures at two selected pressures 0.55 and 3.6 GPa, respectively. Two main features can be highlighted comparing the evolution and the main characteristics of the LP and HP forms. (*a*) The most obvious change occurs along the c-stacking axis by compression of the inter-chain space. (*b*) Limiting the Co—O distance to d < 2.5 Å, the main difference between the LP and HP analogs relies on the Co—O7 bond [~3.1 Å for BCAO at 0.55 GPa, see Fig. 1(*d*)] that enters in the coordination sphere of the CoO_6 octahedra in HP form [~2.1 Å for BCAO at 3.6 GPa, see Fig. 1(*e*)]. It is emphasized in Fig. 6(*d*), by plotting the evolution of d(Co—O) bond distance above P_c. Concerning the Co–Co distances, only the in-chain ones (intra-dimer and inter-dimer) show a significant elongation across P_c. Plots for additional distances are displayed in Fig. S6.

Concerning the pyro-As_2O_7 groups, the As–As distance is nearly unchanged with increasing pressure [see Fig. 6(*a*)], as are the two bridging As—O bonds, while the terminal one shows a jump at the transition related to their orientation along specific unit-cell parameters. The evolution of the Co—O, Ba—O and Co—O distances is given in Figs. 6(*b*), 6(*c*) and 6(*d*), respectively, and corresponding calculated wavenumber values following Badger's rules (Badger, 1934) are discussed below.

3.1.5. Towards non-modulated HP phases. Keeping in mind that the modulation mainly corresponds to out-of-phase undulations between neighbouring chains in the (*a*, *c*) plane with a distribution of compact and relaxed inter-chains areas [see Fig. 1(*c*)], its disappearance above *Pc* matches perfectly with the evolution of the experimental unit-cell parameters. In that sense, one expects a severe contraction along *c* due to the flattening of the chains, which will in turn cause an elongation along the *a* axis. These intuitive features are also in good agreement with the main evolution of the interatomic distances obtained after DFT relaxation, notably concerning the abrupt change in $CoO_{5+1} \rightarrow CoO_6$ coordination.

To further confirm this scenario, we will now address the question of the stability of the modulation in the HP phase. We already highlighted that using our experimental setup, the observation of modulated satellites on powder XRD data failed, so we used DFT calculations to probe it. DFT structural relaxation were performed using 7*a*, *b*, 2*c* commensurate approximant models [due to the high number of individual atoms for all models (28 Ba + 56 As + 28 Co + 196 O), the convergence criteria were lowered to the values given in the experimental section] and by using three different models as follows.

Model 1 corresponds to the 7*a*, *b*, 2*c* (14×) expansion of the ambient-pressure cell (fixed cell) built from translation of the average primitive cell into a supercell. In contrast of the primitive cell (1*a*, 1*b*, 1*c*) approach where this average model easily converged; in the supercell, the ΔE between two iterations remain in the 0.1–0.5 $\times$ 10^{-1} eV range and atomic forces reach up to 0.04 eV Å^{-1} far above a stable crystal structure. The calculations have been re-launched several times but never converged. Similar results have been obtained for model 2, a similar supercell, but built from an undulated model similar to what shown in Fig. 1(*c*). This latter was constructed using the modulated model and corresponds to a particular projection along the fourth dimension of the incommensurate model 14-fold approximant in the real space. For both models 1 and 2, the lowest energy structures are smoothly undulated, but their high relative free energy highlight the inexact commensurate approximation, which for instance fully neglects the non-zero components of the **q** wave vectors along the *b* axis. For model 3, we used the unit-cell parameters refined at 3.1 GPa (fixed cell values) and the 14-times translation of the average primitive structure. The refinement converged promptly within our energetic and force criteria. The examina-

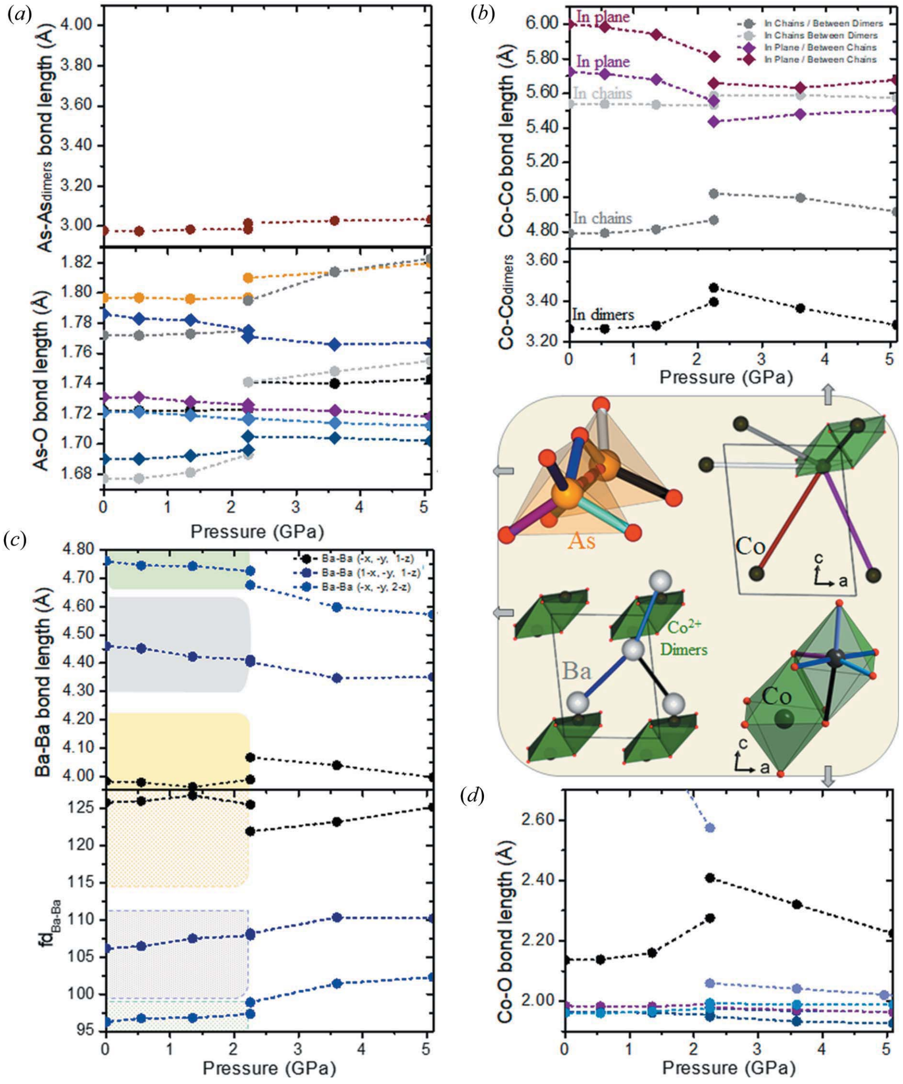

Figure 6

Evolution of selected bond lengths (Å) *versus* pressure (GPa) values extracted from DFT structural relaxation calculations (starting from synchrotron XRD experiment structural models) for BCAO (unit-cell parameters for DFT were constrained to the refined values) for: (*a*) As—As dimers (top) and As—O (bottom), (*b*) Co—Co, (*c*) Ba—Ba and (*d*) Co—O. The coloured squares correspond to the observed amplitude of distances along the modulation. (*c*, bottom) converted values of Ba—Ba bond lengths into equivalent wavenumbers following Badger rules.

tion of the refined model confirms the stabilization of a unique primitive-like motif 14 times repeated with minor deviation between elementary motifs in the supercell at 3.1 GPa. By comparison between the previous attempts, one can conclude a thermodynamical stable non-modulated model at this pressure, and by extension above P_C.

3.2. Raman spectroscopy

The Raman signature of $BaCoX_2O_7$ (X = As, P) compounds were recorded, at atmospheric pressure and room temperature, before starting the high-pressure experiments as presented in Fig. 7. The spectra can be described considering three different regions such as the high wavenumber part between 580 and 1300 cm^{-1}, the low wavenumber part below 120 cm^{-1} and the intermediate part in between. The high wavenumber part corresponds to the vibrations of the phosphate double tetrahedra molecular unit and is independent of the symmetry of the crystal structure. There are some similarities in the high wavenumber part with that found in many other compounds having diphosphate units such as $BaMgP_2O_7$ (Idrissi *et al.*, 2004) and α-$Co_2P_2O_7$ (Harcharras *et al.*, 2003).

Based on the literature, the most intense modes of the P_2O_7 molecular double tetrahedra unit consist of two (symmetric and antisymmetric) stretching modes between 700 and 1000 cm^{-1} that involve the P—O bond of the P—O—P bridging the two tetrahedra, and two, symmetric and antisymmetric, stretching modes between 1000 and 1300 cm^{-1} that involve the P—O bond of the PO_3 tetrahedra (Blanc *et al.*, 2018; Zhang & Brow, 2011; Baran *et al.*, 1986). These modes are indicated by arrows in Fig. 7 in order to sketch the correspondence in wavenumber between P_2O_7 and As_2O_7.

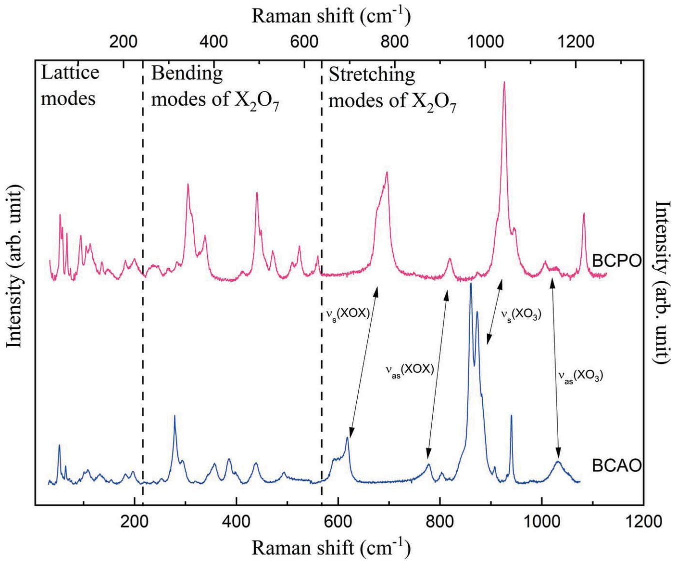

Figure 7
Raman spectra of BCPO and BCAO recorded at atmospheric pressure and room temperature. The three frequency divisions, separated by dashed lines, represent lattice modes of $BaCoX_2O_7$ (X = As, P), bending modes of X_2O_7 (X = As, P) double tetrahedra unit and stretching modes of X_2O_7. BCPO scale belongs to the upper x axis and BCAO scale belongs to the lower x axis.

The molecular vibrational modes are found at a lower wavenumber in BCAO in comparison to BCPO. This can be explained by the larger atomic mass of As compared to that of P and the reduced bond length in the double tetrahedron molecular unit, as well as the fact that the force constant of the As—O bond is smaller than that of P—O (Hanuza *et al.*, 1972).

Additional modes of lower intensity can be observed in this region depending on the symmetry of the molecular unit. For instance, if the angle between the tetrahedra is modified, then the P_2O_7 symmetry could be enhanced, and the total number of modes would be reduced accordingly. The intermediate wavenumber region is composed of a mix between molecular bending modes and other lattice modes and will not be considered in this study. Finally, the most interesting part is the low wavenumber region composed of lattice modes involving heavy alkaline and transitional metal ions such as Ba and Co atoms and of torsional modes of the tetrahedra below 70 cm^{-1} (Hanuza *et al.*, 1972; Idrissi *et al.*, 2004).

The pressure evolution of the Raman signature of $BaCoX_2O_7$ compounds on compression up to 14.1 GPa and 16.6 GPa for BCAO and BCPO, respectively, are displayed in Figs. 8(*a*)–8(*f*). The two colours in Fig. 8 are used to separate the LP and HP phases at 1.8 GPa (BCAO) and 6.8 GPa (BCPO). The pressure dependence of the individual Raman wavenumber obtained by deconvoluting the spectra in the low and high-wavenumber regions is presented in Figs. 9(*a*)–9(*d*).

Remarkably, the low wavenumber region in Figs. 8(*a*) and 8(*d*) display similar pressure evolutions for both compounds. The phase transitions are marked by a jump of mode 1 and 3 and simultaneous disappearance of mode 2 and appearance of

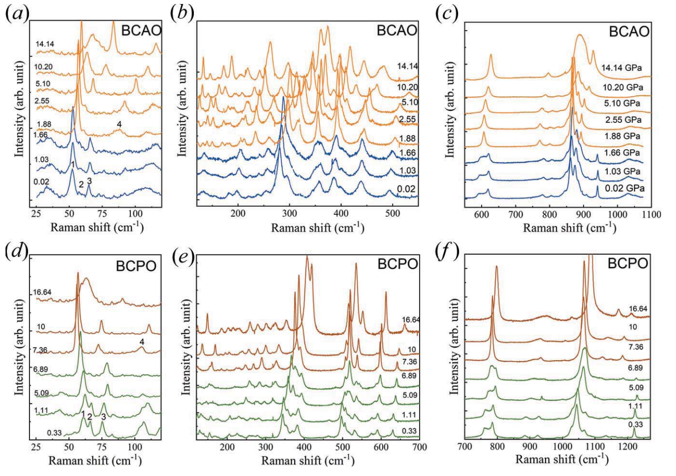

Figure 8
Evolution of the Raman spectra measured in BCAO and BCPO at selected pressures are shown in three different regions with different scaling. Raman spectra at different pressures recorded on compression. Representative Raman spectra of barium cobalt arsenate on compression up to 14.14 GPa: (*a*) between 25 and 120 cm^{-1}, (*b*) between 120 and 580 cm^{-1} and (*c*) high-frequency region between 580 and 1080 cm^{-1}. Representative Raman spectra of barium cobalt phosphate on compression up to 16.64 GPa: (*a*) between 25 and 160 cm^{-1}, (*b*) between 120 and 700 cm^{-1} and (*c*) high-frequency region between 700 and 1280 cm^{-1}. The two-colour representation is used to distinguish between the low-pressure and the high-pressure phases.

mode 4. Thus, from a spectroscopic point of view, the same phase transition occurs in both compounds. In BCPO, the low wavenumber modes 1, 2, and 3 first harden at low pressure (typically below 3 GPa) and then display a progressive softening while approaching the transition. In BCAO however, mode 1 and 3 harden in contrast to mode 2 that soften up to the transition. Notice that at the phase transition, mode 1 shows an upward jump in BCAO whereas it shows downward jump in BCPO. Besides, after the phase transition, mode '1' of BCAO and BCPO are located at the same position, around 55 cm^{-1} in both compounds. Above the transition, a continuous increase of the wavenumber of all modes with increasing pressure is observed up to the highest measured pressure.

In the structure, the shortest Ba–Ba distances (between 4 and 5 Å) in BCPO are smaller than those in BCAO, while the other distances between Co and Co or Co and Ba, are similar in both structures. The Raman modes observed below 100 cm^{-1}, *i.e.* modes 1, 2, and 3 at 65, 60 and 52 cm^{-1} in BCAO and at 75, 65 and 60 cm^{-1} in BCPO are in good agreement with the relative Ba—Ba distances between both compounds [Fig. 6(*c*, top)]. This is clearly shown in Fig. 6(*c*, bottom) which represents the pressure evolution of ideal wavenumber position of the stretching mode of Ba—Ba bonds, based on Badger's rules (Badger, 1934) and the Ba–Ba distances obtained by DFT for BCAO. Although it is not trivial to assign modes across the transition, attempts are proposed in Fig. 9(*a*) and 9(*b*), with positive or negative shift at the transition related to decrease or increase of associated distances, respectively. In BCAO, for which the distance dependence with pressure is more drastic, we found that the calculated evolution of the mode frequencies is in surprisingly good agreement with the experimental Raman modes, see Fig. 6(*c*, bottom) against Fig. 9(*a*). The mode labelled 4 is not assigned yet. Thus, we believe that those low wavenumber modes involve mainly the Ba network. At the transition, for BCPO we observed negative shifts for both modes 1 and 3, which suggest an increase of most of the short Ba–Ba distances at the transition in this compound. This might be explained looking at the evolution of the unit-cell parameters of BCPO, see again Fig. 4(*b*), by the predominant *a*-dilatation at the transition while the unit-cell parameters *b* and *c* evolve almost continuously.

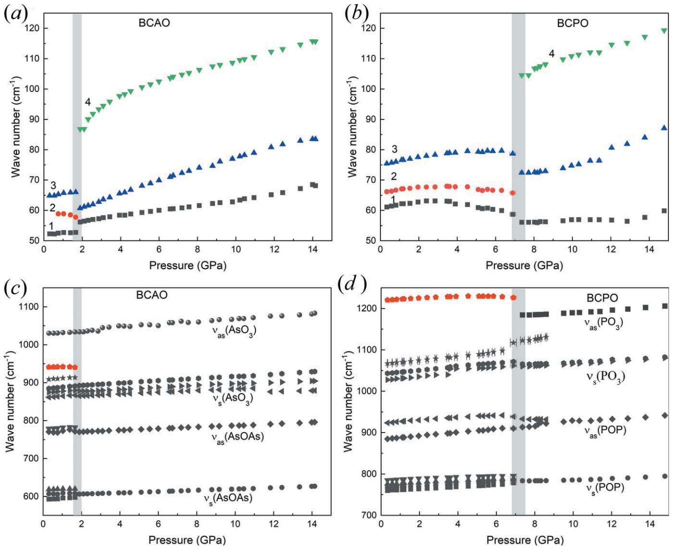

Figure 9
Evolution of four different low-frequency phonon modes with pressure which are named 1 to 4 for (*a*) BCAO and (*b*) BCPO. The evolution of high-frequency regions with several phonon modes associated with symmetric and antisymmetric vibration with pressure for (*c*) BCAO and (*d*) BCPO. A sharp phase change can be observed around 2 GPa in the plot. Similarly, a phase transition can be observed around 7 GPa pressure, where the phonon-mode position changes drastically. The error bars are of the same order of magnitude as the symbol size.

As mentioned in earlier section the high wavenumber region (higher than 550 cm^{-1}) is exclusively composed of Raman modes that involve stretching of the X—O bond either in XO_3 or in a X—O—X bridge between two tetrahedra that form the double tetrahedral $(X_2O_7)^{4-}$ unit. In these two compounds, like in other diphosphate compounds (Edhokkar *et al.*, 2014), the two symmetric and two antisymmetric vibrations follow the energy hierarchy $\nu_s(XOX) < \nu_{as}(XOX) < \nu_s(XO_3) < \nu_{as}(XO_3)$. Note that the antisymmetric stretching vibrations are always challenging to observe in Raman spectroscopy and are more intense using IR spectroscopy, but we believe that they are located at 1030 cm^{-1} in BCAO and 1150 cm^{-1} in BCPO; and adopt a regular wavenumber shift with increasing pressure.

Rulmont *et al.* (1991) stated that for a given molecular vibration (XOX bridge or X—O bond length in XO_3) the splitting between symmetric and antisymmetric modes can be related to the angle between the two tetrahedral XO_4 units. In BCPO compound, we applied Lazarev's relationship, $\Delta = (\nu_{as}\text{POP} - \nu_s\text{POP})/(\nu_{as}\text{POP} + \nu_s\text{POP})$ and using the plot (Fig. 3 of the reference) given by Rulmont *et al.* (1991); we find Δ*100 in the range of 8.27 to 8.38 in the pressure values from 9.5 GPa to 16.64 GPa. This implies that the angle between the two tetrahedral XO_4 units does not vary much in the pressure range explored during our experiment and therefore that the double tetrahedra are not destroyed under the application of high pressure.

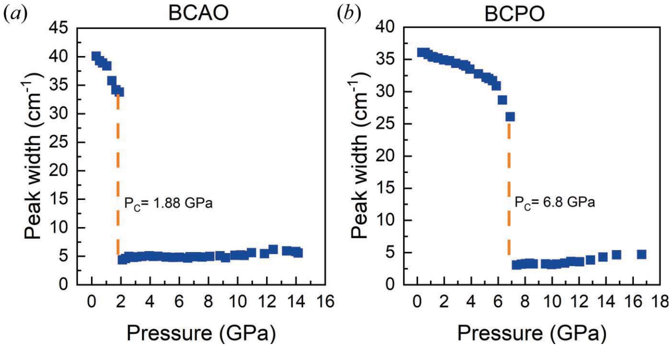

Figure 10
Pressure evolution of peak width of the symmetric (XOX) Raman mode of (*a*) BCAO and (*b*) BCPO, which present fingerprint of first-order phase transition. The error bars are of the same order of magnitude as the symbol size.

The pressure dependence of the symmetric (XOX) Raman modes at 600 cm^{-1} in BCAO and 680 cm^{-1} in BCPO, in Figs. 8(*c*) and 8(*f*), show an expected hardening with increasing pressure. In both compounds, these modes display an abnormal square shape, and this feature has not been observed before in other diphosphate (diarsenate) compounds with non-modulated structures; this is reminiscent of a superposition of several peaks at different positions. With increasing pressure, these modes transform into a single line at the transition pressure in both BCAO and BCPO compounds. As exemplified in Figs. 10(*a*) and 10(*b*) (for BCAO and BCPO, respectively), the peak width of the symmetric stretching vibration of the $X{-}O{-}X$ bridges of the double tetrahedral molecular units shows an abrupt and huge reduction at 1.88 GPa and 6.8 GPa for BCAO and BCPO, respectively, which can be taken as a very accurate way of determining the phase transition pressure.

Identical simplification of the symmetric (XO) Raman mode between 880 and 1050 cm^{-1} is also observed at the phase transition. The intensity of the majority of the peaks enhances with increasing pressure. Moreover, another fingerprint of the phase transition is associated with the disappearance of the narrow Raman mode observed at 941 cm^{-1} in BCAO and 1080 cm^{-1} in BCPO.

Finally, when looking at the low wavenumber region (< 55 cm^{-1}) in Fig. 8(*a*), we observe a torsional mode at 45 cm^{-1} that displays a 10 cm^{-1} continuous softening with increasing pressure up to the transition for BCAO. The same low wavenumber mode is also observed in BCPO, which can be seen in Fig. 11(*a*). The wavenumber variation with pressure follows a classical critical law often observed during displacive phase transitions see Fig. 11(*b*) (Hanuza *et al.*, 1972).

From Raman spectroscopy, we can conclude these significant points:

(i) The phase transition is detected at 1.8 GPa for BCAO and 6.8 GPa for BCPO as evident from the sudden narrowing of the symmetrical X_2O_7 (X = P, As) molecular unit Raman modes at high wavenumber. We observed these features for the first time to the best of our knowledge.

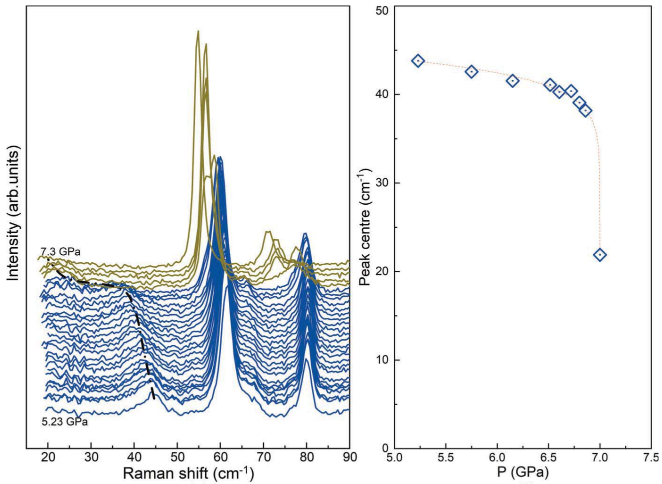

(*a*) (*b*)

Figure 11
Observation of soft mode in BCPO at very low-frequency regime: (*a*) Raman spectra of low wavenumber region measured with several steps during decompression, the black dot-dotted line indicates the soft mode position; (*b*) evolution of the soft mode phonon frequency with pressure.

(ii) The phase transition is accompanied by the disappearance of narrow bands that are observed only in modulated structures.

(iii) The first-order transition is confirmed from the sharp jump observed in low wavenumber Raman modes.

(iv) The torsional mode at very low wavenumber (< 45 cm^{-1}) follows a critical softening that reveals the partly displacive nature of the transition.

3.3. Origin of the pressure-induced phase transition

We have seen that the analysis of DFT-relaxed models based on the evolution of the unit-cell parameters experimentally obtained by synchrotron XRD measurements gives consistent arguments for the vanishing of incommensurate structural modes at the pressure phase transition P_c: (i) elongation of the a axis along the chains direction, (ii) simultaneous contraction of the c axis which is the main direction of the modulated atomic displacement and (iii) evolution of the interatomic distances toward more regular coordination (for instance $CoO_{5+1} \rightarrow CoO_6$). This is further shown by Raman spectroscopy. Indeed, the symmetric modes at 580–620 cm^{-1} in BCAO and 750–800 cm^{-1} in BCPO transform to a single peak at the critical phase transition P_c for both compounds. The unusual square shape of these modes observed in the starting modulated phase is not observed in other non-modulated monoclinic diphosphate phases (Blanc *et al.*, 2018); thus we believe that this unusual shape is a result of the modulation that also impacts on the X_2O_7 molecular chain in the structure. The sudden narrowing of the width to the single vibrational mode at the transition shows that the molecular unit adopts a more symmetrical packing as a result of the disappearance of the modulation. This is a highly sensitive way of detecting the modulation in this type of structure to the best of our knowledge. This means the modulation in the heavy atoms is also sensed in the molecular X_2O_7 units. We have also observed a very sharp mode marked with red pentagon symbols in Figs. 9(*c*) and 9(*d*) at ~940 cm^{-1} in BCAO and ~1223 cm^{-1} in BCPO that disappear at the phase transition pressure. Again, this modification of the intensity of such a Raman mode is a fingerprint of the change in the molecular units' arrangement in connection with the disappearance of the modulation.

4. Conclusions

In this study, $BaCoX_2O_7$ (X = As, P) compounds were investigated as a function of hydrostatic pressure using synchrotron diffraction and Raman spectroscopy supported by DFT structural calculation. Synchrotron XRD measurements reveal a reversible first-order pressure-induced phase transition at 1.8 GPa for BCAO and 6.8 GPa for BCPO with a discontinuity in the unit-cell parameters and a phase coexistence regime. The low and high wavenumber regions of

Raman spectra carry the fingerprints of the phase transition, such as the appearance of new Raman modes at low wavenumber, sudden reduction of multiple Raman lines to a single line at the phase transition, and disappearance of Raman lines in high wavenumber region. The disappearance of the modulation in the high-pressure phase is clearly observed by the variation of the shape of the symmetric XOX stretching at 600 cm^{-1} that involves XO bonds in between two tetrahedra units. The high-pressure phase exhibits simplification of the number of Raman modes (to a single mode) and demonstrates the connection between the modulation of heavy atoms and the molecular X_2O_7 anionic unit. Remarkably the local site is modified because of some antisymmetric stretching XO mode that disappears at the transition pressure. Finally, the very low wavenumber torsional modes display a critical law that is often found in displacive transitions. We interpret this as a modification of a specific vibrational property (a torsion of each P_2O_7) of the molecular unit whose torsion is also affected by the phase transition.

In conclusion, many fingerprints of the disappearance of the incommensurate structural modulation of these compounds with hydrostatic pressure were captured by the analysis of Raman spectroscopy. DFT calculations further confirm this scenario. Besides the atypical flattening of drastically undulated 1D units, it is an important issue because the modulation mediates the multiferroicity in this family. Further efforts will be initiated to investigate how the disappearance of this incommensurability changes the type of stabilized magnetic structure and how this affects the electrical properties.

Acknowledgements

The authors want to thank C. Felix (POM), A. Prat (X'press), R. Bruyère (X'press), Ch. Bouchard (X'press), M. Legendre (X'press) and S. Douillet (AutoCarac) for their technical support at Institut Néel. We thank SOLEIL for the synchrotron beamtime on PSICHE beamline (proposal 20191619) and Nicolas Guignot for his kind help with the pressure chamber imaging during the experiment.

Funding information

This work was carried out under the framework of the LOVE-ME project supported by the ANR (Grant ANR ANR-16-CE08-0023).

References

Badger, R. M. (1934). *J. Chem. Phys.* **2**, 128–131.

Baran, E., Botto, I. & Nord, A. (1986). *J. Mol. Struct.* **143**, 151–154.

Blanc, N. A., Williams, Q., El Bali, B. & Essehli, R. (2018). *J. Am. Ceram. Soc.* **101**, 5257–5268.

Blöchl, P. E. (1994). *Phys. Rev. B*, **50**, 17953–17979.

Canévet, E., Grenier, B., Klanjšek, M., Berthier, C., Horvatić, M., Simonet, V. & Lejay, P. (2013). *Phys. Rev. B*, **87**, 054408.

Carlson, S. & Krogh Andersen, A. M. (2001). *J. Appl. Cryst.* **34**, 7–12.

Colmont, M., Darie, C., Tsirlin, A. A., Jesche, A., Colin, C. & Mentré, O. (2018). *Inorg. Chem.* **57**, 6038–6044.

Colmont, M., Zadoya, A., Darie, C., Domingos, C., Leclercq, B. & Mentré, O. (2021). *CrystEngComm*, **23**, 5124–5130.

David, R., Kabbour, H., Colis, S., Pautrat, A., Suard, E. & Mentré, O. (2013). *J. Phys. Chem. C*, **117**, 18190–18198.

Edhokkar, F., Hadrich, A., Mhiri, T. & Graia, M. (2014). *Crystallogr. Rep.* **59**, 937–943.

Finger, L. W., Cox, D. E. & Jephcoat, A. P. (1994). *J. Appl. Cryst.* **27**, 892–900.

Gonzalez-Platas, J., Alvaro, M., Nestola, F. & Angel, R. (2016). *J. Appl. Cryst.* **49**, 1377–1382.

Hanuza, J., Jeżowska-Trzebiatowska, B. & Łukaszewicz, K. (1972). *J. Mol. Struct.* **13**, 391–403.

Harcharras, M., Ennaciri, A., Capitelli, F. & Mattei, G. (2003). *Vib. Spectrosc.* **33**, 189–196.

Holzapfel, W. B. (2003). *J. Appl. Phys.* **93**, 1813–1818.

Hyatt, N. C., Gray, L., Gameson, I., Edwards, P. P. & Hull, S. (2004). *Phys. Rev. B*, **70**, 214101.

Idrissi, M. S., Rghioui, L., Nejjar, R., Benarafa, L., Idrissi, M. S., Lorriaux, A. & Wallart, F. (2004). *Spectrochim. Acta A Mol. Biomol. Spectrosc.* **60**, 2043–2052.

Klotz, S., Chervin, J. C., Munsch, P. & Le Marchand, G. (2009). *J. Phys. D Appl. Phys.* **42**, 075413.

Koepernik, K. & Eschrig, H. (1999). *Phys. Rev. B*, **59**, 1743–1757.

Kresse, G., Marsman, M. & Furthmüller, J. (2012). *Vienna Ab Initio Simulation Package (VASP), The User Guide*. Universität Wien. http://www.vasp.at/.

Laugier, J. & Bochu, B. (2002). *CELREF*. Unit-cell refinement software on a multiphase system. Laboratoire des Matérériaux et du Génie Physique, Ecole Nationale Supérieure de Physique de Grenoble (INPG), France.

Leclercq, B., Arévalo-López, A. M., Kabbour, H., Daviero-Minaud, S., Pautrat, A., Basu, T., Colin, C. V., Das, R.-R., David, R. & Mentré, O. (2021). *Adv. Quant. Techn.* **4**, 2000064.

Lenertz, M., Dinia, A., Colis, S., Mentré, O., André, G., Porcher, F. & Suard, E. (2014). *J. Phys. Chem. C*, **118**, 13981–13987.

Momma, K. & Izumi, F. (2008). *J. Appl. Cryst.* **41**, 653–658.

Perdew, J. P., Burke, K. & Ernzerhof, M. (1996). *Phys. Rev. Lett.* **77**, 3865–3868.

Prescher, C. & Prakapenka, V. B. (2015). *High. Pressure Res.* **35**, 223–230.

Riou, D., Labbe, P. & Goreaud, M. (1988). *C. R. Acad. Sci. Paris*, **307**, 903–907.

Rodríguez-Carvajal, J. (2001). *IUCr Commission on Powder Diffraction Newsletter*, No. 26, pp. 12–19.

Rulmont, A., Cahay, R., Liegeois-Duyckaerts, M. & Tarte, P. (1991). *Eur. J. Solid State Inorg. Chem.* **28**, 207–219.

Singh, K., Maignan, A., Pelloquin, D., Perez, O. & Simon, C. (2012). *J. Mater. Chem.* **22**, 6436–6440.

Wojdyr, M. (2010). *J. Appl. Cryst.* **43**, 1126–1128.

Zhang, L. & Brow, R. K. (2011). *J. Am. Ceram. Soc.* **94**, 3123–3130.